Advancements in Non-Destructive Archaeometric Analysis of Ancient ferrous artefacts: Insights from SR-X-Ray Diffraction investigation using model alloys

Leila Galai, Emilie Bérard, Solenn Réguer, Eddy Foy, Cristian Mocuta, Caroline Toffolon-Masclet, Thomas Guilbert, Philippe Dillmann

Advancements in Non-Destructive Archaeometric Analysis of Ancient ferrous artefacts: Insights from SR-X-Ray Diffraction investigation using model alloys

Authors: Leila Galai (1), Emilie Bérard (2), Solenn Réguer (3), Eddy Foy (1), Cristian Mocuta (3), Caroline Toffolon-Masclet (4), Thomas Guilbert (5), Philippe Dillmann (1)

(1) Laboratoire Archéomatériaux et Prévision de l'Altération : IRAMAT UMR7065 CNRS et NIMBE UMR3685 CEA/CNRS, Université Paris-Saclay, CEA Saclay, Gif-sur-Yvette, France

(2) Université Paris-Saclay, CNRS, ICMMO, Orsay, France

(3) Synchrotron SOLEIL, Saint Aubin, France

(4) Université Paris- Saclay, CEA, DES/ISAS/DRMP/S2CM/LM2T, Gif-sur-Yvette, France

(5) Université Paris- Saclay, DES/ISAS/DRMP/SRMA/LA2M, Gif-sur-Yvette, France

Abstract:

The exploration of archaeological heritage aims at understanding past societies through the study of ancient materials. While archaeometric analysis provides valuable insights, invasive sampling raises ethical concerns and is often restricted, necessitating the development of non-invasive techniques. This study presents a methodology based on X-Ray Diffraction using synchrotron radiation. The approach involves the elaboration and characterization of model alloys, with X-ray data analysis using Rietveld refinement and Williamson-Hall plot method. Phase identification along with crystallographical investigations conducted on three medieval armours provides insights into manufacturing techniques and highlights the method's limitation.

Keywords: SR-XRD, Medieval armours, Non-invasive techniques, model alloys.

1. Introduction

The exploration of our historical and archaeological heritage has long been linked with the quest for understanding the material remains of past societies. In this purpose, archaeometric analysis emerges as a pivotal tool to complement textual and archaeological evidences, offering profound insights into the material composition, provenance, and the History of Techniques [1-4]. However, the common practice used in archaeological sciences based on extracting samples raises ethical concerns on these invaluable artifacts due to its invasive nature and is often not authorized by museums. As we explore deeper into ancient societies and given the physico-chemical heterogeneity of cultural heritage material, the importance of developing non-invasive characterization techniques becomes increasingly necessary [5]. These techniques not only preserve the integrity of archaeological objects but allow to multiply

the analyses, significantly increasing the representativeness of the results on the whole artefact.

In this context, the study of iron-based metallic artifacts is of great interest to document the history of techniques, craft organization and skills transmission. Metallographic analysis, commonly used among archeometallurgists [1, 3, 6-9], offers detailed informations about the microstructure, phase composition, and heat treatment history of iron artifacts. As this methodology requires collecting samples, it is essential to develop and implement innovative and non-invasive techniques for the metallurgical study of iron artifacts to broaden the range of information collected.

In this context, non-destructive methods like neutrons diffraction and X-Ray diffraction using Synchrotron Radiation (SR-XRD) offer promising alternatives, preserving the integrity of the objects while providing detailed structural and chemical information. SR-XRD is well suited to analyse the bulk of thin metal artefacts (1 or a few mm, depending on the energy used) [10], while neutron diffraction allows to study thicker samples (around several centimetres) [5, 11-17].

Thanks to a fast acquisition, SR-XRD can allow multiple analyses on the surface of large size samples (several dozen of centimeters), crucial to evaluate the heterogeneity of an artifact composed of several metal sheets as in the work on Berard et al. [10]. In addition, photon flux, as well as increased beam collimation and monochromaticity compared to classical laboratory X-ray generator, enhance the angular resolution and favor the detection of minor phases such as iron carbides, especially cementite, found in ancient steels.

In continuation of a previous work [10], this approach addresses the examination of crystallographic structures, phase identification, and quantitative phase analysis on three medieval armour pieces and on specific model alloys, representative of commonly encountered microstructures in ancient ferrous alloys using SR-XRD and Rietveld and Le Bail Refinements.

2. Experimental sections

2.1 Materials

2.1.1 Model alloys

a. Production and characterization of high-purity ingots

Three ingots with targeted carbon content of 0.3 wt. %, 0.5 wt.% and 0.7 wt.% were fabricated. The ingots were produced by melting a mixture of high-purity iron and carbon powders (Fe Neyco-99,99% in purity, 3-6 mm (batch FC102275-Fe) and C graphite Neyco-99,99% in purity 1-6 mm (batch 102275-C)) using induction heating under an inert atmosphere (Ar). To ensure a complete homogenization, the ingots were re-melted and flipped five additional times.

Carbon content were estimated using Combustion Infrared Absorption (CIR) (EMIA-Pro and EMIAExpert Carbon/Sulfur Analyzers, Horiba), and minor elements were measured by X-ray fluorescence using Niton Xl3t portable XRF analyzer from Thermo Fisher Scientific with an Ag anode under 50 kV high voltage and a beam size of 3 mm diameter. The chemical composition of the ingots is presented in Table 1. It should be noted that during the production of FeC0.3%, the ingot was unintentionally cooled more quickly than the other ingots.

Table 1. Chemical composition measurements by Combustion Infrared Absorption (C) and XFR (W, Cu, Cr and As) in wt.%.

	FeC 0,3 wt.%	FeC 0,5 wt.%	FeC 0,7 wt.%
C	0,29 ± 0,01	0,48 ± 0,01	0,68± 0,01
W	0,097	0,122	0,08
Cu			
Cr		<0,1 wt. %	
As			

b. Heat treatments applied on model alloys

The controlled heat treatments were conducted on parallelepipedic samples (8 x 8 x 2 mm^3) using a DT-1000 dilatometer. This dilatometer gives access to a wide range of cooling rates, from 0.5 °C/s to 400 °C/s, using a cryogenic system with liquid nitrogen. The thermocouple welded to the sample surface ensures perfect control of the programmed thermal cycle. The heat treatment procedure (Fig.1) involves a heating phase with a 10°C/s heating rate until reaching the austenization temperature at 875°C for 5 minutes. This was followed by a cooling step at different rates, depending on the targeted microstructures. The cooling rates applied are the following ones: 0.5, 5, 10, 100 and 400 °C/s, covering a wide range of cooling rates: slow, fast and intermediate. These cooling rates were selected to cover the range of cooling rates for water quenching, oil quenching, and air cooling. According to the IRSID database [18], water quenching cooling rates exceed 100°C/s, oil quenching rates range from 10°C/s to 100°C/s, and air cooling rates fall between 0.1°C/s and 10°C/s. This broad spectrum ensures the representation of most microstructures and the understanding of the thermal cycles that led to their formation. Through instrumented heat treatments, a precise control is carried out over the process. The model samples are designated hereafter according to the formalism FeCx-y, where x refers to the target C content (0.3 wt.%, 0.5 wt.% and 0.7 wt.%) and y refers to the cooling rate applied in °C/s.

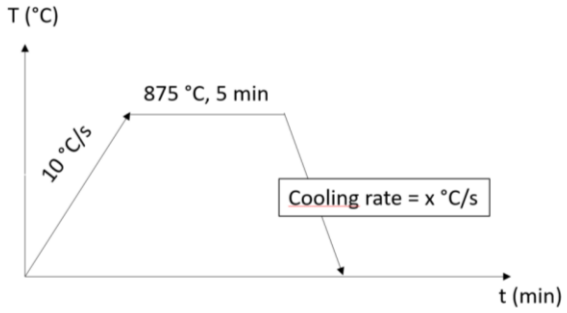

Figure 1. Applied heat treatment for microstructure generation.

2.1.2 Armour pieces

Three medieval armour pieces, a back plate (PO679.2), a left chest plate (PO679.1) and a visor (PO664) belonging to the Musée de l'armée (Paris, France) were analyzed by SR-XRD (Fig. 2). The three pieces are supposed to have been made in Italy. Two of them, (PO679.2 and PO679.1) are part of a large medieval arms and armour Hoard found in Chalcis (Euboea Island, Greece) [19-21] and are covered with a black surface coating. Our aim was to document the technical skills of the craftsmen and highlight any manufacturing specificities. Concerning the back plate, a small part was slightly and manually polished (until 4000 grade SiC paper) for XRD analysis in order to avoid the detection of corrosion products and eventually the black surface treatment applied. The left chest plate was analyzed on the edge, after polishing. The visor piece was analyzed without any preliminary treatment on two positions, P1 and P2 (see Supplementary information section). For pieces PO679.2 and PO679.1, unpolished areas were also analyzed, revealing the signal of the black surface coating mixed with corrosion products. Hence very localized areas were slightly polished to directly analyze the metallic matrix.

Table 2. Specifications of the analyzed armour pieces.

Identification Number	Category	Date	Assumed place of fabrication	Marks	Additional information
PO679.2	Large plate from brigandine	1380	Italy	-	Belong to the Chalcis Hoard
PO679.1	Large plate from brigandine	1380	Italy	S surmounted by a crown	Belong to the Chalcis Hoard

PO664	Sallet	mid 15th century	Italy	AM surmounted by a crown	

Figure 2. Back plate "PO679.2" (a), left chest plate "PO 679.1" (b) and visor "PO664" (c) zoom view on marks applied on the reverse side of PO 679.1 (d), zoom view on marks on visor "PO664" (d).

2.2 Characterization techniques for the heat-treated model alloys

After the thermal treatments, the samples were polished using SiC papers firstly, then with 3 µm and 1 µm diamond suspensions. Before metallographic observation, the samples were etched with 3% nital to reveal the grain boundaries and microstructures. Metallographic observations (MO) were conducted using an Olympus Optical Microscope (BX51 model) and a Secondary Electron (SE) imaging with Scanning Electron Microscopy (SEM) (Zeiss Merlin). Vickers micro-hardness of the samples was measured using a BUEHLER VH3300 durometer with a mass of 200g held during 10 seconds.

2.3 Synchrotron X-Ray Diffraction

X-ray diffraction measurements were performed at the Synchrotron SOLEIL, on the DiffAbs beamline, at room temperature, on model alloys as well as armour pieces. The monochromatic X-rays are obtained using a Si(111) double crystal monochromator (bandpass of $\Delta E/E \sim 10^{-4}$). Two 50 nm rhodium-coated Si single crystal mirrors were employed to effectively reject higher X-rays harmonics by a cumulated factor of about 10^{-6}. The beam is focused in vertical

(longitudinal bending of the mirrors) and horizontal directions (sagittal bending of the second crystal of the monochromator) respectively, resulting into a beam size of about 160 × 250 μm^2 (FWHM, vertical × horizontal). The photon flux at the focal spot reached several 10^{11} ph/s for the used photon energy of 17.97 keV.

A curved hybrid pixel area detector (CirPAD) consisting of 20 modules [22] was used to acquire diffractograms over up to 135° scattering angle range (Fig. 3a). For each sample, the diffractogram was the result of the average of at least ten images (each one obtained after 30 s exposure time) of the same analyzed area of the sample. The aim was to fill in the inter-module gaps. After the alignment of the samples within the beam, an incidence angle of 9° was applied generating a beam footprint of about 1280 x 160 μm^2. After the measurements, specific treatment was performed on each portion, equivalent to one module, to obtain a continuous diffractogram. The XRD pattern of LaB_6 reference powder in capillary was also measured for CirPAD geometry calibration and determination of the exact wavelength was made using Rietveld refinement. The samples were aligned on the X-ray beam in two different set ups depending on the sample type, i.e the amour pieces and the model alloys. The model alloys were placed on a spinner, so that the samples were rotated during the acquisition. However, the complex shapes of the armour pieces and the need for secure analysis prevented their rotation. Instead, the objects were placed in the center of the diffractometer on wide range translation stages allowing for a precise positioning of different area of the armour pieces to be investigated for profiles or punctual measurements. Laser beams were used to help for sample alignment (Fig. 3b). A specific protocol was implemented to study the possible presence of texture in the amour pieces. The available rotation carrying the CirPAD detector [22] was used to map extensive regions of the diffraction rings in angular space to obtain information on sample texture by measuring intensity variations along the diffraction rings azimuthal direction. 2D resulting images are generated thanks to a homemade python code workflow used to reconstruct data acquired with the CirPAD.

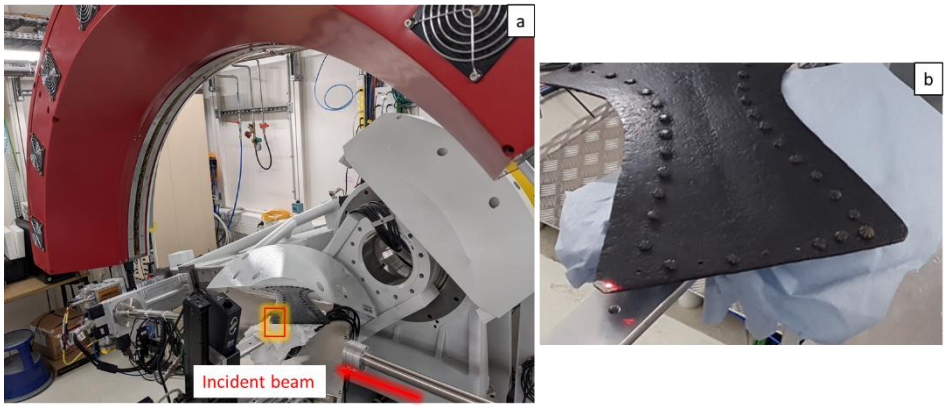

Figure 3. Alignment of the back plate "PO679.2": The red arrow indicates the incident beam (a), with a zoomed -in view (b) to localize the laser pointer) marking the incident beam's impact on the sample.

2.4 Rietveld and Le Bail Refinement

The diffraction diagrams were analyzed using Rietveld and Le Bail (pattern matching) refinements with the software JANA 2006 [23]. The analysis of diffraction diagrams using JANA software involves several key steps to extract detailed structural information from samples. The first step of the refinement consists in defining the background manually. Depending on the microstructure generated, the refinement is performed considering ferrite and cementite phases or ferrite, martensite and/or austenite phases. The corresponding CIF Files were downloaded from ICSD data base[1].

JANA software facilitates the refinement of crystal structures through Rietveld analysis, adjusting parameters to minimize the difference between observed and calculated diffraction patterns. Additionally, the software enables the calculation of microstructural parameters such as the crystallite size and strain using Williamson-Hall analysis, providing insights into the sample's defects and crystallite size distribution. Quantitative phase analysis can be performed to identify the relative amounts of phases present in the samples.

3. Results and discussion

3.1. Models alloys : dilatometry/characterization OM/SEM et Vickers µ-hardness

The complete dilatation curves for all the model alloys are presented in the Supplementary Informations section. The cooling part of each dilatation curve is presented in Fig. 4. According to these dilatation curves, the microstructures have been generated as expected.

- Ferrito-pearlitic microstructure

For the three different carbon content (0.3%, 0.5% and 0.7%) and for the cooling rates of 0.5°C/s, 5°C/s and 10°C/s (Fig.), the ferritic transformation (T_s) begins at temperatures between 752 °C and 665°C (Table 3), indicating the formation of a ferrito-pearlitic microstructure [24]. The starting temperature (T_s) of the ferritic transformation (Fe-γ→Fe-α) decreases as the cooling rate increases. At a slower cooling rate, thermodynamic equilibrium is more easily reached, allowing transformations to occur at higher temperatures, close to the equilibrium temperature. As the cooling rate increases, austenite is undercooled. The temperature of the material drops below the temperature at which the transformation would normally have started at equilibrium. T_s also decreases with the increase of carbon content, as carbon is an austenite stabilizer: it has a high solubility in austenite (γ-Fe) compared to ferrite (α-Fe). Austenite becomes more stable than ferrite, thereby lowering the temperature at which ferrite begins to form.

[1] https://icsd.products.fiz-karlsruhe.de/

Microstructural examinations using optical microscope and SEM (Fig. 5a1-h1, 5a2-h2, and 5 a3-f3) reveal the presence of pearlite; a two-phase microstructure consisting of alternated layers of α-ferrite and cementite [24-25]. The size of the pearlite lamellae tends to decrease as the cooling rate increases and as the carbon content in the alloys rises, related with the T_s decrease. At lower cooling rates, the carbon and iron have more time to diffuse and form thicker and more widely spaced pearlite lamellae. When cooling rate increases, the transformation from austenite to pearlite occurs more rapidly, at lower temperature, leading to the formation of numerous nucleation sites and a refinement of the lamellae. Consequently, the hardness of the materials increases due to the greater interface between ferrite and cementite. Microhardness increases from Hv 114 for FeC0.3%-0.5 to Hv 339 for FeC0.7%-10.

At a cooling rate of 100°C/s, Fe-C alloys with 0.3% and 0.5% carbon contents display a fine pearlite microstructure. However, for the alloy containing 0.7% carbon, both dilatometric curve (Fig. 4c) and microscopic observations (Fig. 5-g3) indicate that two different transformations have occurred. The dilatometric curve exhibits two inflection points: the first at 526°C, likely corresponding to a ferrite-pearlite or bainite microstructure, and the second one at 245°C, indicating martensitic start transformation. Microscopic observations reveal a martensitic matrix along with a nodular or radial microstructure that could be attributed to pearlite [26] or bainite [27, 24]. Besides, this alloy shows very high hardness (743 HV).

- Martensitic microstructures

At 400°C/s cooling rate, the dilatometric curves of the three different model alloys exhibit a martensitic start temperature at 340 °C, 287°C and 236°C, respectively. The martensitic transformation occurs when the quenching rate is fast enough to prevent carbon diffusion. Martensite is a non-equilibrium phase that results from a diffusionless transformation of austenite [25]. Microscopic observations show the presence of a lath-like microstructure typical of a martensitic microstructure (Figure 5i1,i2 and i3). Microhardness measured for FeC-0.3%-400, FeC-0.5%-400 and FeC-0.7%-400 are 534 HV, 600 HV and 804 HV, showing the increase of martensite hardness with the increase of the carbon content. This increase occurs because, when quenched, the carbon atoms cause significant distortion in the crystal structure, resulting in a body-centered tetragonal (bct) lattice [24]. This distortion makes plastic deformation more difficult, thereby increasing hardness [25]. Heat treatments of model alloys using dilatometry allowed generating various typical microstructures such as ferrito-perlitic or martensitic microstructures. The presence of residual austenite is also likely for these samples.

In addition to the characterization of model alloys using MO, SEM, and Vickers microhardness, a comparison was made with available literature data for alloys of similar composition. CCT diagrams of the C32 and XC 70 alloys, as presented by Murray, 1998 [24], show good

agreement with our results. This confirms the various microstructures obtained for the model alloys, as summarized in Table 3. The obtained microstructures are then used as references during SR-XRD analyses.

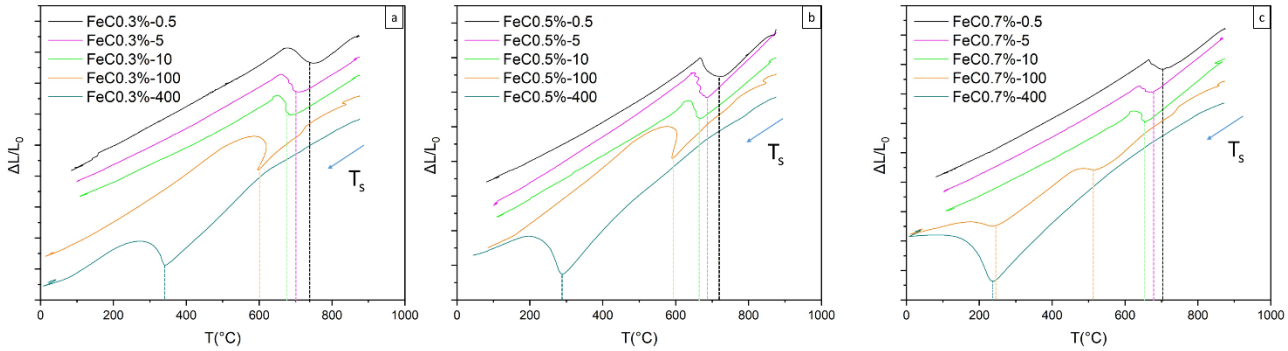

Figure 4. The cooling part of the dilatometric curves obtained for FeC0.3-y (a), FeC0.5-y (b) and FeC0.7-y (c).

Table 3. Ferritic transformation (T_s) and martensitic transformation (M_s) temperature for the model alloys. "F", "P", "M" and "γres" referes respectively to ferrite, pearlite, Martensite and residual austenite.

Cooling rate\ carbon content	0.3%		0.5%		0.7%		microstructure
	T_s	M_s	T_s	M_s	T_s	M_s	
0.5	752		728		721		F+P/ α+Fe_3C
5	705		686		672		
10	681		667		665		
100	597		590		526	245	0.3 wt. % and 0.5 wt. %: F+P/ α+Fe_3C 0.7 wt. % : (F+P) or B +M/ (α+Fe_3C)+ α'
400		340		287		236	M / α' + γres + α

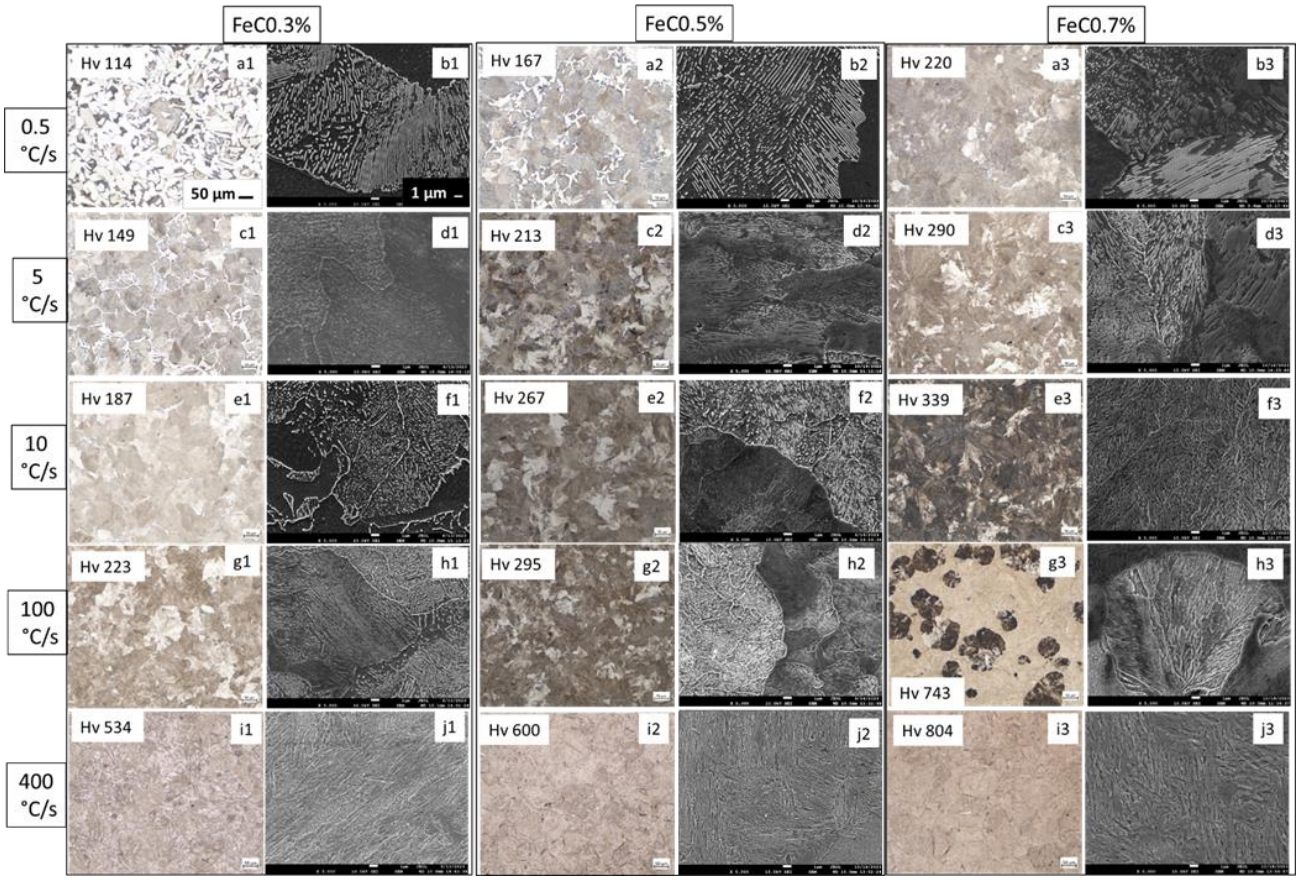

Figure 5. MO and SE SEM images of FeC0.3%-y, FeC0.5%-y and FeC0.7%-y model samples. Vickers microhardness values are given in white boxes inserted in MO images. The scale bars for MO and SEM images are given in a1 and b1, respectively.

3.2. SR-XRD analysis of model alloys

XRD patterns for the FeCx-y model alloys are presented in Fig.6, 7 and 8. For model alloys with 0.3%,0.5% carbon content cooled at 0.5°C/s, 10°C/s and 100°C/s (Fig. 6a-c, 7a-c) and for model alloys containing 0.7%C cooled at 0.5°C/s and 10°C/s (Fig. 8a-b) the presence of cementite peaks (JCPDS #98–2869) indicate the presence of ferrito-pearlitic microstructure observed in section 3.1. Cementite peaks observed in samples cooled at 0.5°C/s (Fig. 6a, Fig. 7a, and Fig. 8a) are better defined and sharper compared to those obtained on samples cooled at 10°C/s (Fig. 6b, Fig. 7b, and Fig. 8b) and 100°C/s (Fig. 6c, Fig. 7c). For slow cooling rates, cementite forms near equilibrium, leading to a more organized crystal structure. Conversely, at higher cooling rates, the crystal structure is less organized, leading to more diffuse diffraction and therefore less well-defined peaks [28-29]. FeC0.7%-100 sample (Fig. 8c) as well as model alloys cooled at 400°C/s (Fig. 6d, Fig. 7d and Fig. 8d) exhibit more broad peaks corresponding to the presence of martensite. The presence of residual austenite is also detected for these samples. For FeC0.7%-100 sample, although microscopic observations revealed the presence of nodular pearlite or bainite within a martensitic matrix, cementite peaks were not detected by XRD, likely due to the enlargement of martensite peaks. The volume fraction of the nodular microstructure containing the carbides seems to be too low to be correctly detected.

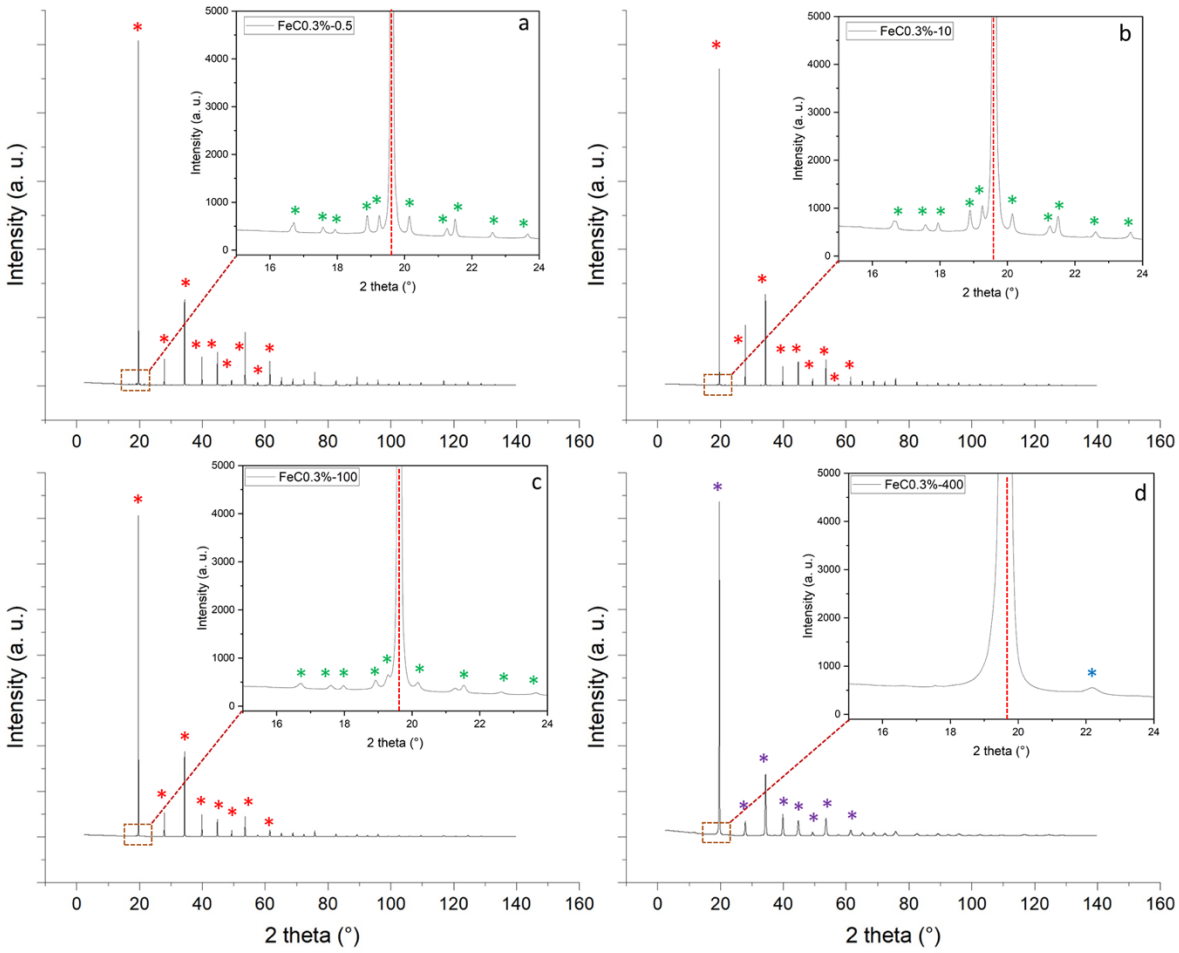

Figure 6. SR-XRD patterns recorded on FeC0.3%-0.5 (a), FeC0.3%-10 (b), FeC0.3%-100 (c) and FeC0.3%-400 (d). The insets correspond to a zoom on the 15-25 2 theta range. The peaks marked by green stars, red stars, blue stars and violet stars correspond to cementite (JCPDS #98–2869), Ferrite (JCPDS #06–0696), Austenite (JCPDS #23–0298), and Martensite (JCPDS #44-1291), respectively.

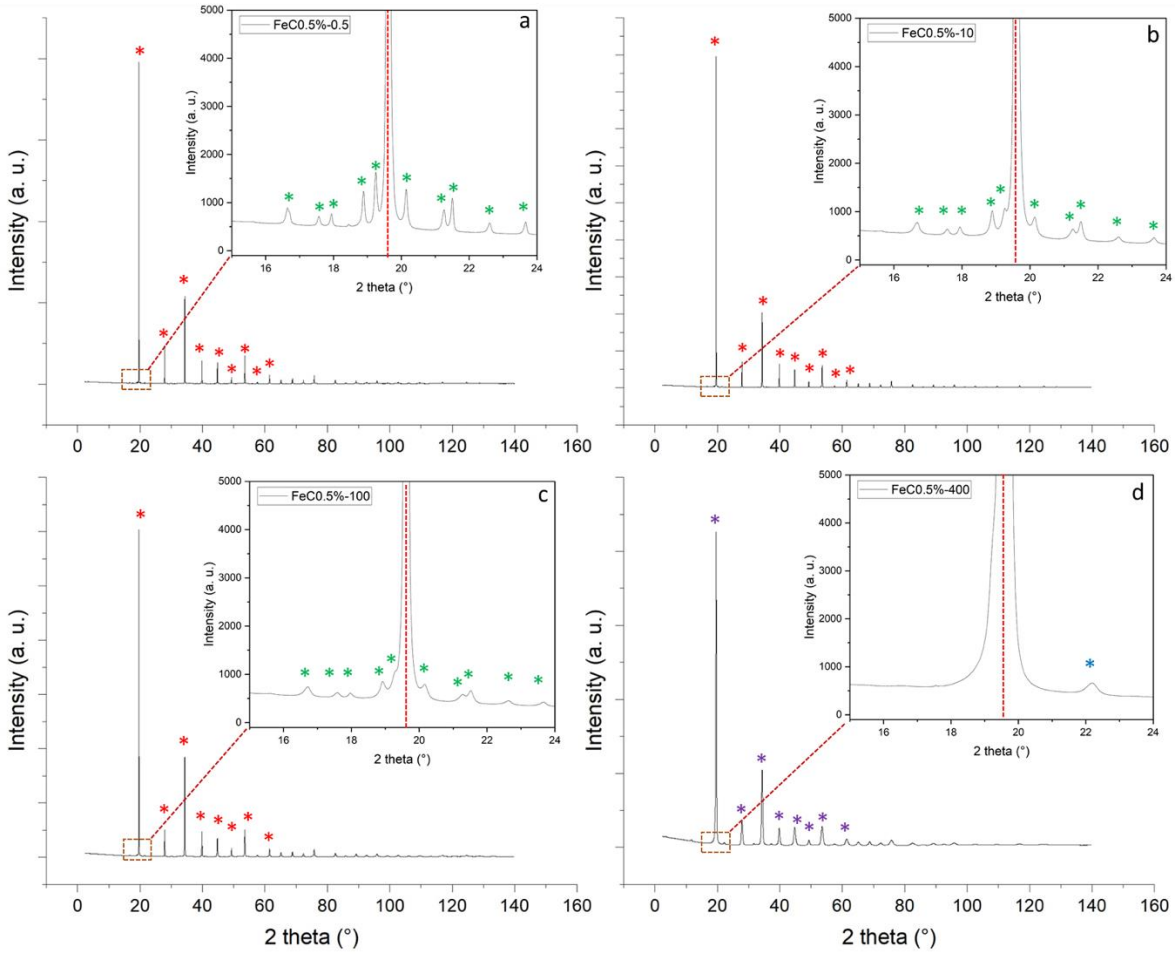

Figure 7. SR-XRD patterns recorded on FeC0.5%-0.5 (a), FeC0.5%-10 (b), FeC0.5%-100 (c) and FeC0.5%-400 (d). The insets correspond to a zoom on the 15-25 2 theta range. The peaks marked by green stars, red stars, blue stars and violet stars correspond to cementite (JCPDS #98–2869), Ferrite (JCPDS #06–0696), Austenite (JCPDS #23–0298), and Martensite (JCPDS #44-1291), respectively.

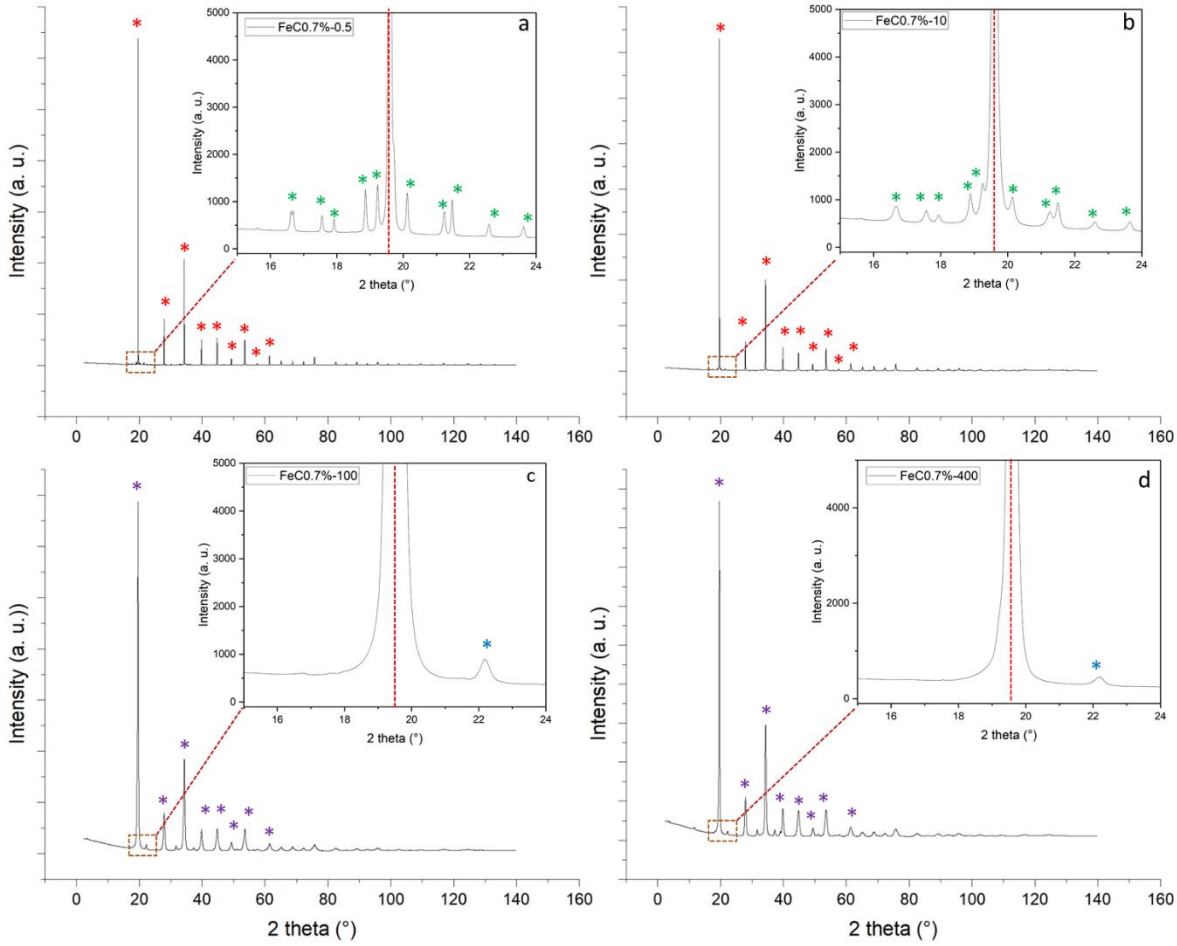

Figure 8. SR-XRD patterns recorded on FeC0.7%-0.5 (a), FeC0.7%-10 (b), FeC0.7%-100 (c) and FeC0.3%-400 (d). The insets correspond to a zoom on the 15-25 2 theta range. The peaks marked by green stars, red stars, blue stars and violet stars correspond to cementite (JCPDS #98–2869), Ferrite (JCPDS #06–0696), Austenite (JCPDS #23–0298), and Martensite (JCPDS #44-1291), respectively.

3.3. Microstructural analysis : FWHM evolution and Williamson and hall plot analysis

For peak shape analysis, pattern matching by Le Bail refinement was conducted on the model alloys prepared for this study. Overall, the refinement was satisfying, except for the FeC0.7%-100 sample, likely due to the presence of a mixed structure. This sample is no further discussed starting from here. The table below details the number of phases used for the refinements, their crystallographic structure, as well as the reliability factors (R_p and R_{wp}) obtained for each sample.

Table 4. Crystallographic structure Le Bail Refined parameters of model alloys.

Sample	Phase	structure space group	R_p (%± 0,01)	R_{wp} (%± 0,01)
FeC0.3%-0.5	Ferrite Cementite	body-centered cubic Im-3m orthorombic Pnma	2.79	5.42
FeC0.3%-5			2.69	4.24
FeC0.3%-10			2.99	5.92
FeC0.3%-100			2.33	4.65
FeC0.5%-0.5			2.5	4.3
FeC0.5%-5			1.88	3.43
FeC0.5%-10			2.13	3.66
FeC0.5%-100			2.12	4.58
FeC0.7%-0.5			2.65	4.84
FeC0.7%-5			1.73	3.19
FeC0.7%-10			2.25	3.71
FeC0.3%-400	Ferrite Martensite	body-centered cubic Im-3m body-centered tetragonal Pmna	2.86	4.36
FeC0.5%-400			2.53	4.62
FeC0.7%-400			3.61	5.82

The Full Width at Half Maximum (FWHM) values for the ferrite phase were extracted for each sample, after correction for the instrumental resolution function, and plotted in Fig. 9. An example of the data correction is presented in Supplementay Information section (Fig. A2 and Fig. A3). Model alloys cooled at 400°C/s with a martensitic microstructure (dark cyan symbols) exhibit significantly higher FWHM values compared to samples cooled at lower cooling rate. Martensite formation is a diffusionless process, leading to significant amount of internal stresses, higher dislocation densities and lattice distortions within the microstructure [24]. These factors cause broadening of XRD peaks, resulting in higher FWHM values.

For model alloys with ferrito-pearlitic microstructures, the FWHM values increase with higher cooling rates, as well as with higher carbon content (Fig.9b). The increase in cooling rate induces internal stresses that lead to an increase of FWHM values. Higher cooling rates result in a more refined pearlite microstructure with smaller cementite and ferrite layers, as shown by microscopic observation (section 3.1). The increase of the amount of grain boundaries and interfaces in a refined microstructure acts as additional sources of strain. Besides, smaller

crystallite sizes induced by faster cooling rates also cause a broadening of the diffraction peaks, thereby increasing the FWHM [30-32]. In order to better quantify these differences on peak broadening between model alloys, further peak broadening analysis has been made using the Williamson and Hall method.

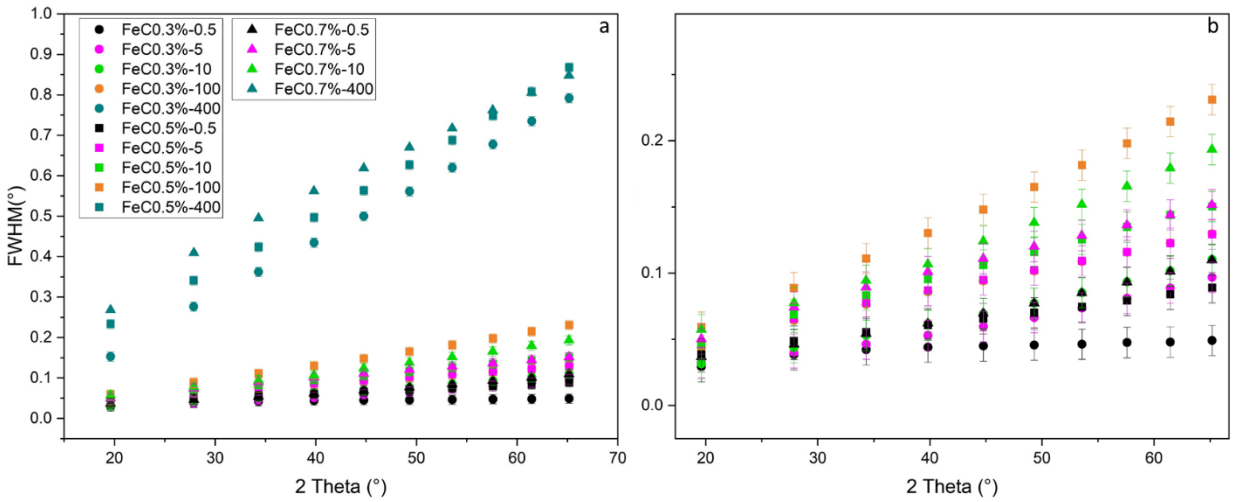

Figure 9. Evolution of FWHM in 2 theta as a function of the scattering angle (2 theta, photon energy = 17.97 keV) for the model alloys (a), zoom on the lower cooling rates (b).

3.2.2. Microstructural analysis: Williamson-Hall plot analysis

The Williamson-Hall method is an analytical technique used in X-ray diffraction (XRD) to determine both crystal crystallite sizes and microstructural deformations in a material [30-31]. This method analyzes the broadening of the diffraction peaks which can be attributed to the size of the crystallites and to the deformations of the crystal lattice [30]. The simplifying hypothesis underlying the Williamson-Hall diagram consists in considering that all contributions have a Lorentzian character. Williamson-Hall equation is expressed as follows:

$$\beta = \beta^T + \beta^D \quad \text{(Eq. 1)}$$

β , the observed FWHM, is the sum of the elementary widths induced by each of the effects: the widths linked to the size of the crystallites (β^T) and to the microdeformations (β^D). β^T and β^D are expressed as follows:

$$\beta^T = \frac{\lambda}{L\,cos\theta} \text{ [33]}$$

$$\beta^D = \eta\, tan\theta \quad \text{[34]}$$

where, L is the crystallite size, η is the average strain in the crystal lattice, λ is the wavelength and θ is the scattering diffraction angle. Williamson-Hall equation is then written as follows:

$$\beta\,\frac{cos\theta}{\lambda} = \frac{1}{L} + \eta\,\frac{sin\theta}{\lambda}$$

The plot of $\beta \frac{cos\theta}{\lambda}$ versus $\frac{sin\theta}{\lambda}$ can give access to the strain induced on the particles and crystallite size which are proportional to the slope of the plot and y-intercept, respectively. Fig. 10a shows the W-H plots of the model alloy samples. The deduced strain η for each model alloys is plotted as a function of cooling rate for each carbon content (Fig. 10b) and the deduced grain size is given in Table 4. The uncertainties were estimated by propagation of the error associated with the angular resolution of the device (0.0115° [22]) and the standard error deduced after the linear fitting.

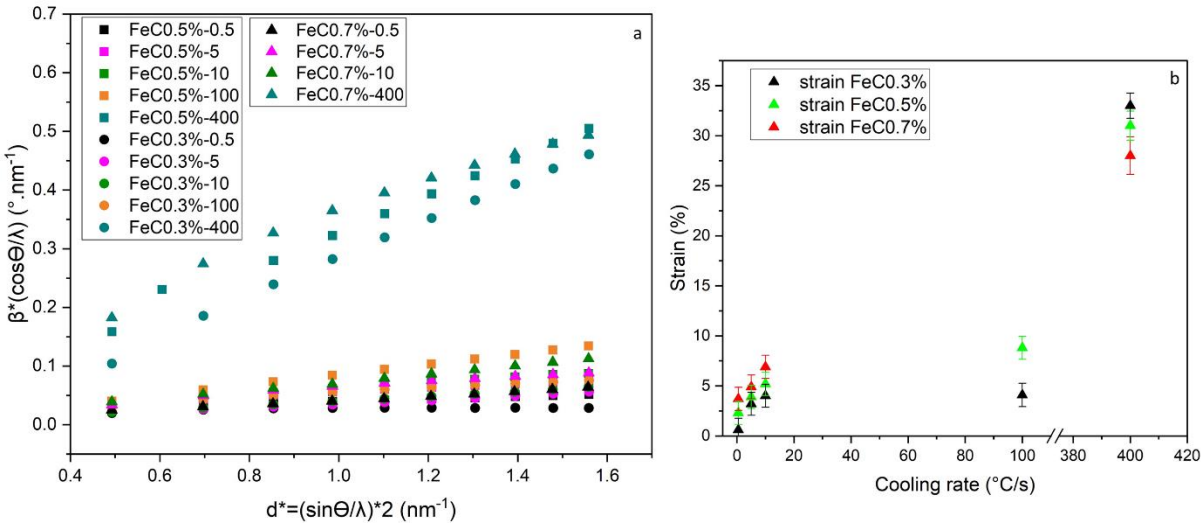

Figure 10. Williamson and Hall plot for model alloys (a), Strain values for model alloys as a function of cooling rate (b).

The evolution of strain confirms that internal stresses and strains increase with the cooling rate in model alloys. Specifically, alloys cooled at 400°C/s with carbon 0.3%, 0.5%, and 0.7% contents exhibit strain values equal to 33% ± 1, 31% ± 1, and 28% ± 2, respectively. In contrast, ferrito-pearlitic microstructures show significantly lower strain values, ranging between 0.6% and 7 %. This indicates that the strain values increase as a function of both cooling rate and carbon content.

Williamson and Hall method also allows determining the crystallite size, as presented in Table 4. For the three carbon contents studied, the crystallite size is smaller for the alloy quenched at 400°C/s (21.2, 49.6 and 13.5 nm) compared to those cooled more slowly [32]. However, no clear trend is observed when comparing the crystallite sizes of the ferrito-pearlitic model alloys. This can be explained by heterogeneous microstructures resulting from non-equilibrium formation, which leads to local variations in composition and grain size. The size value obtained for FeC0.3%-10 and FeC0.5%-100 significantly deviates from the other values. This discrepancy likely occurs because the device has reached its resolution limit, preventing accurate quantification of larger crystallite sizes (micron level), thereby introducing higher uncertainty.

Table 4. Size and strain results for the model alloys.

Cooling rate\ carbon content	0.3%		0.5%		0.7%	
	Size (nm)	Strain %	Size (nm)	Strain %	Size (nm)	Strain %
0.5	48.3 ± 5	0.6 ± 1 %	61.7 ± 3	2 ± 1 %	194.1 ± 12	4 ± 1 %
5	260.4 ± 38	3 ± 1%	63.4 ± 8	4 ± 1 %	66.8 ± 14	5 ± 1 %
10	900.9 ± 611	4 ± 1 %	104.9 ± 21	5 ± 1 %	299.4 ± 46	7 ± 1 %
100	74.1 ± 12	4 ± 1 %	1029 ± 946	9 ± 1 %		
400	21.2 ± 3	33 ± 1 %	49.6 ± 25	31 ± 1 %	13.5 ± 3	28 ± 2

The Williamson-Hall analysis enables the correlation of cooling rates with induced strain. By applying this methodology to armour pieces, we aim at suggesting the specific cooling rates employed. This approach allows a better understanding of the microstructural characteristics and mechanical properties of the armour, which are essential for understanding heat treatment history of iron artifacts.

3.4. Quantitative analysis : comparison of carbon contents determined by Rietveld refinements with carbon contents measured by CIR

For ferrito-pearlitic microstructures, the weight fraction of ferrite ($f_{Fe-\alpha}$) and cementite (f_{Fe_3C}) are proportional to the relative intensities of the diffraction peaks. Quantitative multiphase was performed using Jana2006 software in order to determine the relative weight percent of ferrite and cementite. From the relative proportion of cementite with respect to the surrounding matrix, it is possible to determine the carbon content ($C\ [wt\%]$) using the following equation:

$$C\ [wt\%] = 0.02 \times f_{Fe-\alpha}[wt\%] + 6.67 \times f_{Fe_3C}[wt\%] \quad \text{(Eq.2)}$$

The carbon content determined using this method is compared to the value measured by CIR, along with the reliability factors (R_p and R_{wp}) for each sample (Table 5). The results obtained for FeC0.3% significantly deviate from the experimental measurement. The method was ineffective for 0.3% alloys. The reason of this is not yet fully understood and might require further examinations. For model alloys containing 0.5 wt.% and 0.7 wt.% C, the results indicate that for 0.5°C/s cooling rate, the value deduced by refinements closely matches the value

measured by CIR. However, as the cooling rate increases, the deduced values diverge and becomes lower than the measured ones.

This suggest that, at higher cooling rates, deviation from thermodynamic equilibrium occurs, resulting in a lower quantity of crystallized cementite and a higher strain value. The carbon is likely incorporated into phases not detected by XRD. This could be due to the very small size of these crystallites, generating very broad peaks that may be indistinguishable from background. Additionally, the increase in strain (Table 4), leads to the breaking of crystalline domains, leading to the quantification of fewer crystallized phases. This highlights the challenge of accurately quantifying carbon under non-equilibrium conditions, particularly when dealing with phase mixtures, which is often the case with ancient ferrous alloys.

The method developed in this study, which highlights the correlation between carbon content and strain values, could serve as an indicator when quantifying the unknown carbon contents of museum pieces. Measuring strain values may serve as an indicator of the reliability of carbon quantification. A low strain value could suggest a proximity to thermodynamic equilibrium, leading to a more accurate carbon determination using Rietveld method. Conversely, high strain values may indicate that the carbon content obtained may be less reliable.

Table 5. Deduced carbon contents from Rietveld refinement from the ferrito-pearlitic microstructures of the model alloys.

Wt.%C (CIR)	Cooling rate (°C/s)	Wt.%C (Rietveld) (± 0,1)	Strain	R_p %	R_{wp}
0,29 ± 0,01	0.5	0.79	0.6 ± 1 %	8.94	16.35
	5	0.40	3 ± 1%	11.58	21.11
	10	0.15	4 ± 1 %	12.06	18.26
	100	0.16	4 ± 1 %	9.05	16.19
0,48 ± 0,01	0.5	0.47	2 ± 1 %	6.29	9.68
	5	0.45	4 ± 1 %	7.28	11
	10	0.32	5 ± 1 %	7.49	13.01
	100	0.23	9 ± 1 %	8.96	14.25
0,68 ± 0,01	0.5	0.73	4 ± 1 %	9.51	12.70
	5	0.66	5 ± 1 %	6.73	10.69
	10	0.45	7 ± 1 %	6.9	12.14

3.5. Armour pieces microstructure analysis : XRD analysis and Williamson and hall plot analysis

All the measurements taken on the armour were made in static mode, as it is impossible to rotate the pieces. Rotating the CirPAD detector gives access to the intensity variation of the diffraction rings which can be directly linked to a texture effect. Fig. 11 illustrates some of the representative reconstructed 2D images (one scan of the CirPAD position) obtained for respectively the back plate (PO679.2), the left chest plate (PO 679.1) and the visor (PO 664, position P1 and P2).

Different cases can be observed. Fig. 11a did not show any variation of the intensity along the XRD rings, implying that the material used for the back plate (PO679.2) has few or no texture. Also, no marked texture is detected for the PO 664 whether P1 or P2 position. On the contrary, texture effect is observed on Fig. 11b for which intensity variations on the XRD rings were measured on the side slice of the left chest plate piece (PO679.1).

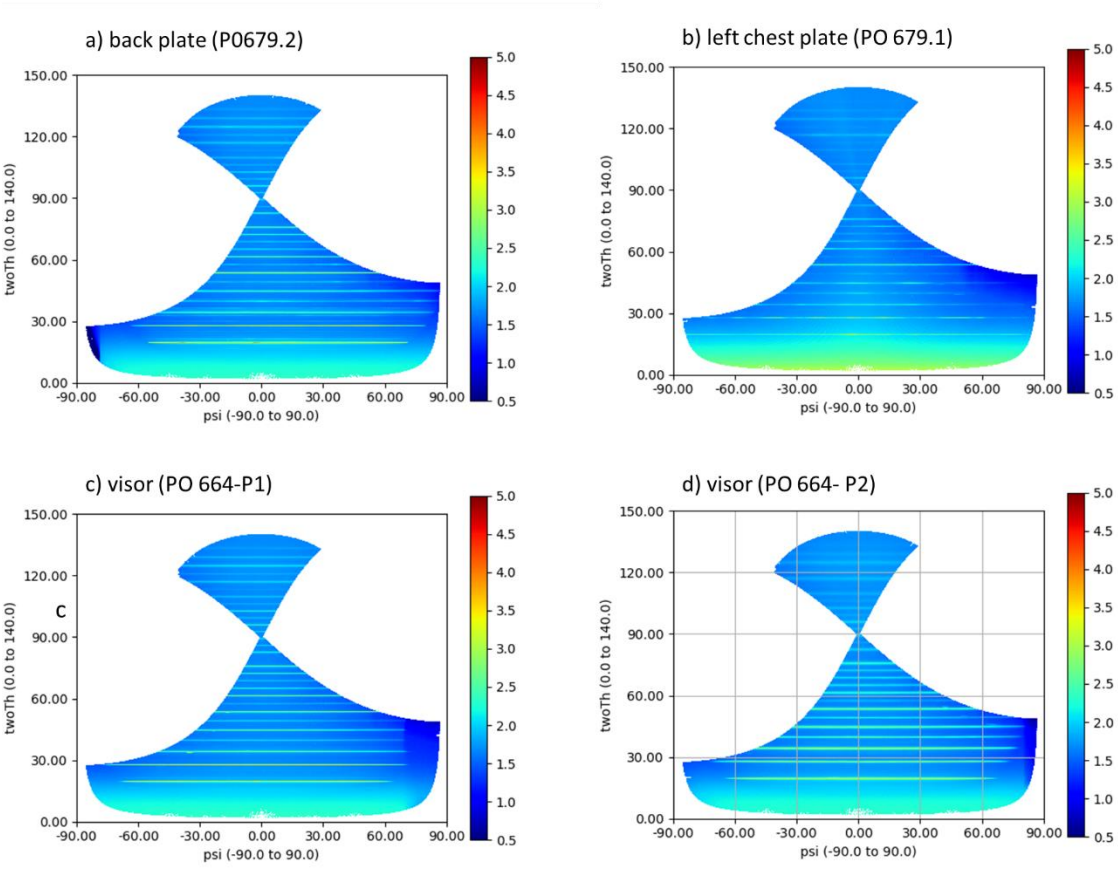

Figure 11. 2D image resulting of the accessed angular map during a measurement with the CirPAD from -25° to + 50° (1° step) showing the intensity (logscale) versus 2 theta (0–135°) versus psi (-90 + 90), revealing the intensity along XRD rings (a) back plate (P0679.2) (b) left chest plate (PO 679.1) (c) visor (PO 664-P1) (d) visor (PO 664- P2). The choice is to show the intensity variation versus 2theta (scattering angle) and psi (azimuth on the XRD ring). Thus, the XRD rings appear as horizontal lines (2theta = constant).

The XRD patterns obtained for the analyzed armour pieces are presented in Fig. 12. Among the analyzed pieces, cementite peaks (JCPDS #98–2869), were identified exclusively on the back plate (PO679.2) (Fig. 12a) and on the visor in position P1 (Fig. 12c), suggesting a ferrito-pearlitic microstructure in these samples. In contrast, the second position analyzed on the visor (Fig. 12d) displayed a significantly different XRD pattern, with no cementite peaks observed and broad peaks at 19.59, 27.84 and 34.27° (Fig. 12d), suggesting a high dislocation density due to the presence of martensitic microstructure or significant hammering not followed by annealing. For the left chest plate piece (PO679.1), the XRD pattern differed again; no cementite peaks were detected and finer ferrite peaks could rather suggest that the material is a very low carbon steel. To better understand the thermal or mechanical treatments applied to these armour pieces, further microstructural analysis using Williamson and Hall methods were applied.

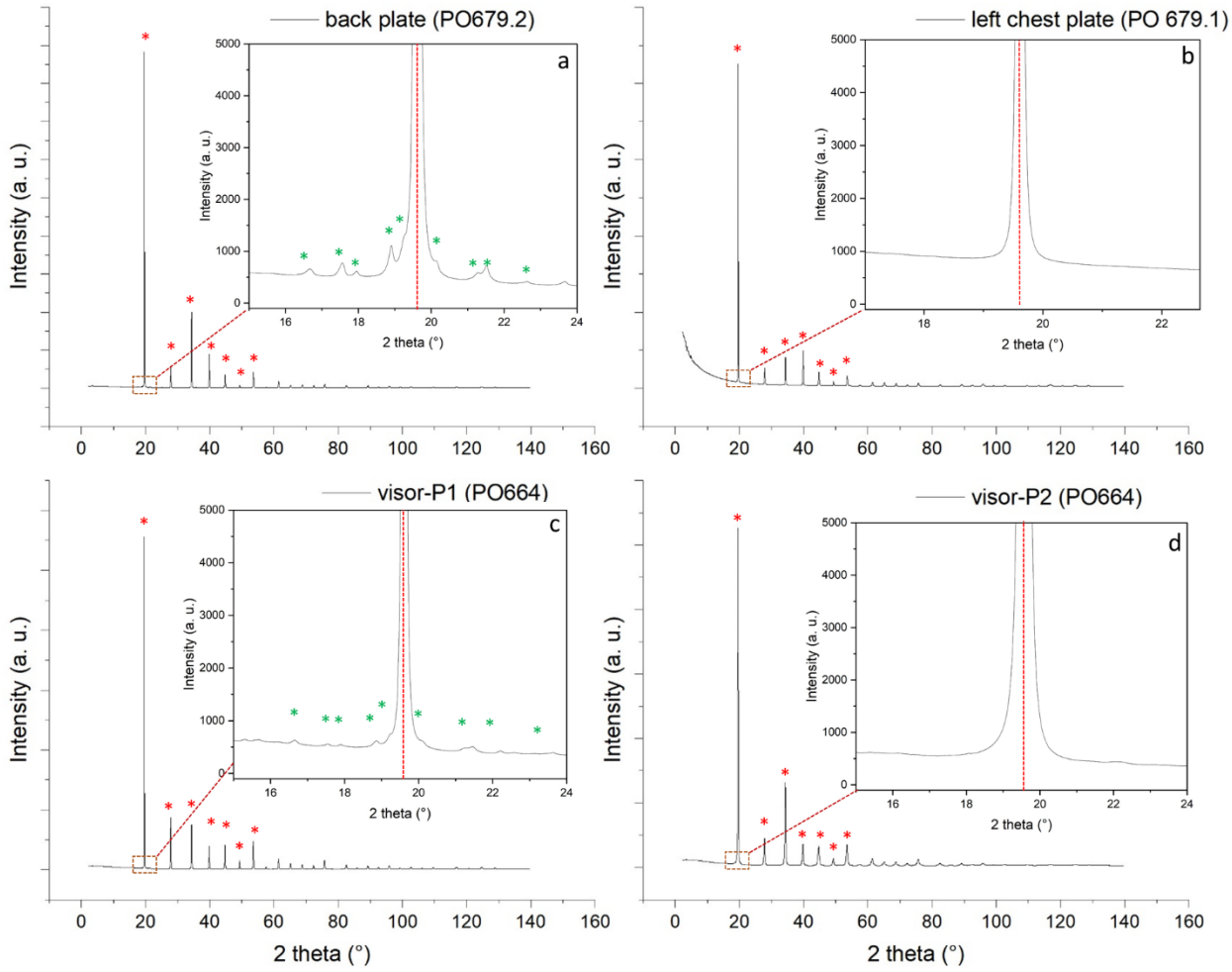

Figure 12. SR-XRD patterns recorded on the armour pieces: back plate PO679.2 (a), left chest plate PO679.1 (b), visor position P1 (c) and visor position P2. The insets correspond to a zoom on the 15-24 2 theta range. The peaks marked by green stars, red stars correspond to cementite (JCPDS #98–2869) and ferrite (JCPDS #06–0696), respectively.

Williamson-Hall analysis was applied to the armour pieces applying the methodology used for model alloys. The refinement fit parameters obtained for the armours are given in Table 6. The results are plotted alongside the model alloys in Fig. 13.

Table 6. Crystallographic structure Le Bail Refined parameters of armour pieces.

Armour piece	phase	structure space group	R_p (%± 0,01)	R_{wp} (%± 0,01)	Strain	Crystallite size	Most probable microstructures	Most probable manufacturing processes
back plate (PO679.2)	ferrite cementite	body-centered cubic Im-3m orthorombic Pnma	2.71	4.76	6 ± 1%	45±10 nm	Ferrito-perlitic	Cooling under conditions faster than thermodynamic equilibrium **Or** Low carbon steel with low work-hardening.
Visor-P1 (PO664)			3.03	5.41	7 ± 1%		Ferrito-perlitic	Cooling under conditions faster than thermodynamic equilibrium **Or** Low carbon steel with low work-hardening.
left chest plate piece (PO679.1)	ferrite	body-centered cubic Im-3m	2.86	4.77	13 ± 1%		Ferrite	Very low carbon steel with rigorous work-hardening/
Visor-P2 (PO664)	martensite	body-centered tetragonal Pmna	3.48	5.84	24 ± 1 %		tempered martensite	Quenching followed by slight tempering /
	ferrite	body-centered cubic Im-3m						

According to strain values, none of the armour samples were cooled following thermodynamic equilibrium conditions. For the back plate piece (PO679.2), the strain deduced from the Williamson-Hall plot analysis is 6 ± 1%. Comparing this value with those obtained for model alloys (Table 4) suggests that the thermal treatment applied to this piece likely involved a slow cooling rate. However, the value is slightly higher compared to the values obtained at 0.5°C/s (0.6 ± 1 %, 2 ± 1 % and 4 ± 1%, for FeC0.3%, FeC0.5% and FeC0.7%, respectively). It may have undergone oil quenching or a delayed quench, However, this hypothesis can not be fully confirmed because air cooling can also lead to 10°C/s cooling rates [18]). Rapid cooling followed by tempering may have also lead to the removing of residual strain and allowing the

formation iron carbides (tempered martensite). Finally, the slightly higher strain value could also suggest the presence of a low-carbon steel with low work-hardening.

The Williamson-Hall plot analysis (Fig. 13a) as well as strain plot (Fig. 13b) for the left chest plate piece (PO 679.1) present strain values between the ones of the quenched model samples and the slowly cooled ones. The deduced strain value (13 ± 1%) is lower compared to those obtained for full martensitic microstructures (~30%). This piece likely mainly consists in a ferrite microstructure that has been shaped and hardened through rigorous work hardening without subsequent annealing [32,11], explaining the high level of strain. Another possibility is that it consists of slighlty tempered martensite, allowing the formation of very fine iron carbides, with a volume fraction being too low to be accurately detected by XRD.

Finally, the visor piece exhibits two different microstructures, linked with two different levels of strain on both analyzed points. For the position P2, Williamson-Hall plot is closer to plot lines corresponding to martensitic model alloy. Besides, the high level of strain (24 ± 1 %) corroborates the hypothesis of a martensitic microstructure in this area leading to a greater hardness of the material. Another hypothesis is that it consists in a very low carbon steel work hardened without subsequent annealing. At position P1, the identified cementite peaks as well as the deduced strain value seems to confirm the ferrito-pearlitic microstructure. To explain this microstructural heterogeneity on the same armour piece, as no visible welding is observed among this piece, it is more likely that it was made from a raw material initially inhomogeneous in term of carbon content, or that the carbon did not spread homogeneously during solidification. Depending on the smithing hearth temperature gradient and the local distribution of carbon content before quenching, heterogeneous microstructures may be generated, composed of several phases. When quenching at a certain cooling rate, carbon-rich regions facilitated the formation of martensite, whereas other areas, containing lower amounts of carbon did not form martensite. This observation is supported by the results from model alloys

cooled at 100°C/s: alloys containing 0.3 wt.% and 0.5 wt.% carbon exhibited a ferrito-pearlitic microstructure, whereas martensite was formed in the alloy containing 0.7 wt.% C.

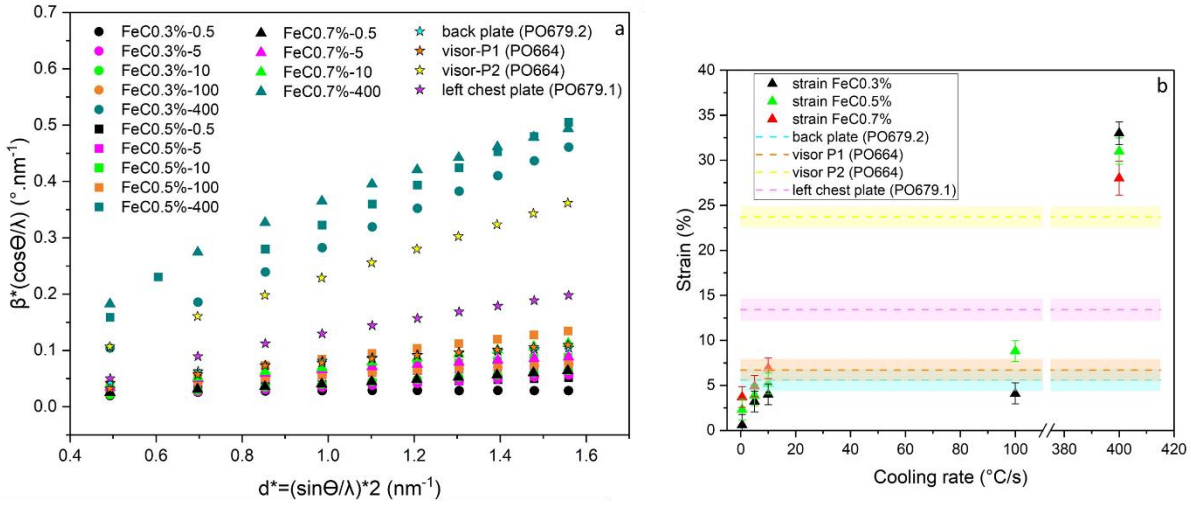

Figure 13. Williamson-Hall plot model alloys and armour pieces (a). Strain values of armour pieces and model alloys plotted in the same graph.

Concerning the carbon content in the analyzed armour pieces, Rietveld refinement was conducted on the diffraction pattern of the back plate (PO679.2) piece. The refinement achieved reliability factors of 11.1% and 16.8 % for R_p and R_{wp}, respectively. The deduced carbon content value from Eq.2 is 0.2 %. However, considering the strain value of 6%, it is likely that the actual carbon content of this piece is higher than 0.2%. This can be further supported by comparing the strain values obtained for this piece with those of model alloys, suggesting that the carbon content of this piece is more likely between 0.3% and 0.5%. Hence caution should be exercised when making quantitative estimates of alloy carbon content using this method, in view of these large discrepancies.

The results show that precise identification of the microstructure based on XRD examination is a delicate task as many parameters are involved (metal composition heterogeneity, cooling rate, work-hardening …). Nevertheless, it is likely that deliberate hardening of the alloys was sought for at least two pieces, showing the highest strain values: left chest plate piece (PO679.1) and the visor (PO664). It could have been achieved by heat-treatment (quenching) or rigorous work-hardening. On this regard, analyses made on pieces PO679.2 and PO679.1, although both belonging to the same hoard, seem to highlight difference in metal supply or hardening-treatments. Based on the developed approach, the multiplication of analyses on a larger number of objects could be of great help in the future to document craftsmen technical skills and choices, depending on the artefact's use.

4. Conclusion

Through the combination of XRD analysis, Rietveld refinement and Williamson-Hall plot analysis based on model alloys and artefact examinations, we have gathered clues to propose hypotheses on the microstructural compositions and on the thermal and mechanical treatments applied to three armour pieces from the Musée de l'Armée (Paris, France). This detailed structural analysis underscores the complex thermal history and mechanical properties of the armour pieces, providing crucial insights into ancient armaments. The analysis of peak shapes has yielded valuable indirect information about microstructures, including average crystallite size and strains. Based on these microstructural insights, we can infer some of the thermal and mechanical processes employed during manufacturing and to highlights crafstmans's intention of conduction hardening operations. This exploration into non-invasive archaeometric analysis marks a significant advancement in archaeological research, promising a deeper understanding of our shared heritage. SR-XRD analysis has particularly proved its efficiency for studying armour samples and other ferrous artifacts, offering a non-destructive mean to gather a wide range of quantitative and meaningful data especially when combining with Rietveld refinement and Williamson and Hall analysis. In the future, the developed approach based on heat treated model alloys could be enriched by the fabrication of work hardened alloys to better discriminate between the manufacturing hypothesis. This study also underscores the challenges of accurately quantifying carbon content in non-equilibrium phases, which is often the case with ancient ferrous alloys.

Authors contribution statement

All authors contributed to the study conception and design. Material preparation and data analysis were performed by Leila Galai. Data collection and analysis were performed by Leila Galai, Emilie Bérard, Solenn Reguer, Eddy Foy, Cristian Mocuta, Caroline Toffolon-Masclet, Thomas Guilbert and Philippe Dillmann. The first draft of the manuscript was written by Leila Galai and all authors commented on previous versions of the manuscript. All authors read and approved the final manuscript.

Data availability

The datasets generated during the current study are available from the corresponding author on reasonable request.

Conflict of interest statement

The authors have no conflict of interests to declare that are relevant to the content of this article.

Funding

This work was supported by the DIM-PAMIR, Ile-de-France Region research network dedicated to the study of heritage sciences.

Acknowldgments

We would like to thank: Olivier Renaudeau (Musée de l'Armée) for allowing studying the armour, and the staff of Musée de l'Armée for logistics , the staff of IPANEMA (Université Paris-Saclay, CNRS, ministère de la Culture, UVSQ, Muséum national d'histoire naturelle USR 3461) for the access to their equipment and storage room, Kevin Ginestar (CEA/DES/ISAS/DRMP/S2CM/LECNA) for the CIR measurements, Amelie Gangloff for the help with SEM observations (CEA/DES/ISAS/DRMP/SRMA/LA2M) and Marc Ronfard-Haret (CEA/ DES/ISAS/ DRMP/SRMA/LTMEX) for the elaboration of ingots.

We acknowledge SOLEIL for provision of Synchrotron radiation facilities and we would like to thank Dominique Thiaudière and Philippe Joly for assistance in using Diffabs beamline (Proposal n° 20230668).

References

[1] G. Pagès, P. Dillmann, P. Fluzin, and L. Long, J. of Archaeol. Sci. 38, 1234 (2011) https://doi.org/10.1016/j.jas.2010.12.017.

[2] Y. BENHIMA, "Quelques aspects de l'historiographie des transferts techniques en Méditérranée médiévale", dans Construire la méditérannée, penser les transferts culturels. Approches historiographiques et perspectives de recherches, München, 2012, p. 148–161.

[3] M. L'Héritier, P. Dillmann, S. Aumard, and P. Fluzin, in The World of Iron, edited by J. Humphris and T. Rehren (Archetype Publications, London, 2013), pp. 409–420.

[4] C. Verna and P. Dillmann, « Histoire des techniques médiévales et cultures matérielles », dans La culture matérielle : un objet en question, 2018, p.127-140.

[5] F. Grazzi, F. Cantini, F. Salvemini, A. Scherillo, B. Schillinger, A. Kaestner, D. Edge, A. Williams,The investigation of Indian and central Asian swords through neutron methods, Journal of Archaeological Science: Reports, 20, 2018, https://doi.org/10.1016/j.jasrep.2018.06.010

[6] A. Williams, The Knight and the Blast Furnace: A History of the Metallurgy of Armour in Middle Ages and the Early Modern Period (Brill, London, 2003).

[7] A. Disser, P. Dillmann , C. Bourgain , M. L'Héritier, E. Vega, S. Bauvais, M. Leroy, J. of Archaeol. Sci. 42 (2014) https://doi.org/10.1016/j.jas.2013.10.034

[8] E. Bérard, P. Dillmann, O. Renaudeau, C. Verna, and V. Toureille, J. Cult. Herit. 53, 88 (2022) https://doi.org/10.1016/J.CULHER.2021.11.008

[9] T. Heal, A. Disser , F. Mercier, G. Sarah, F. Theuws, . Archaeol. Sci. Reports 53 (2024) https://doi.org/10.1016/j.jasrep.2023.104236

[10] E. Bérard, P. Dillmann, S. Réguer, E. Foy, C. Mocuta, E. Vega, J. Braun, C. Toffolon-Masclet, T. Guilbert, I. Guillot, The European Physical Journal Plus (2023). https://doi.org/10.1140/epjp/s13360-023-03916-3

[11] A. Fedrigo, F. Grazzi, A. Williams, A. Scherillo, F. Civita, M. Zoppia J. Anal. At. Spectrom., 2013, 28, 908, https://doi.org/10.1039/c3ja50031d

[12] F. Grazzi, F. Civita & Williams, A. (2011). Ancient and historic steel in Japan, India and Europe, a non invasive comparative study using thermal neutron diffraction. Analytical and Bioanalytical Chemistry, 400, 1493–1500. https://doi.org/10.1007/s00216-011-4854-1

[13] F. Grazzi, L. Bartoli, F. Civita, & M. Zoppi (2009). Neutron diffraction characterization of Japanese artworks of Tokugawa age. Analytical and Bioanalytical Chemistry, 395(7), 1961–1968. https://doi.org/10.1007/S00216-009-3048-6

[14] F. Grazzi, E. Barzagli, A. Scherillo, A. de Francesco, A. Williams, D. Edge & M. Zoppi, (2016). Determination of the manufacturing methods of Indian swords through neutron diffraction. Microchemical Journal, 125, 273–278. https://doi.org/10.1016/J.MICROC.2015.11.035

[15] A. Fedrigo, F. Grazzi, A. Williams, S. Kabra, & M. Zoppi, (2015). Phase composition mapping of a 17th century Japanese helmet. Journal of Analytical Atomic Spectrometry, 30, 707–712. https://doi.org/10.1039/C4JA00390J

[16] J. S. Park, F. Grazzi, A. Scherillo & V. Shinde (2022). Metallographic and neutron diffraction analysis on microstructural evolution and control in ancient Indian high carbon steel. Archaeometry, 64(2), 408–421. https://doi.org/10.1111/ARCM.12724

[17] S. Cho, J. Kim, T. J. Kim, H. Sato, I. Huh & N. Cho, (2021). Neutron imaging for metallurgical characteristics of iron products manufactured with ancient Korean iron making techniques. Nuclear Engineering and Technology, 53(5), 1619–1625. https://doi.org/10.1016/J.NET.2020.11.007

[18] Institut de recherches de la sidérurgie française. (1974). Courbes de transformation des aciers de fabrication française. IRSID.

[19] C. Ffoulkes, R. Traquair, 1911. On italian Armour from chalcis in the ethnological museum at athens. Archaeologia 62, 381–390. https://doi.org/10.1017/S0261340900008225

[20] N.D. Kontogiannis, 2012. Euripos-negroponte-egriboz: material culture and historical topography of Chalcis from Byzantium to the end of the ottoman rule. Jahrbuch Der Osterreichischen Byzantinistik 62, 29–56.

[21] E. Bérard, F. Carò & P. Dillmann, (2024). War and commercial exchanges in the late medieval Aegean: Investigating the metal provenance of the Chalcis Hoard. Journal of Archaeological Science: Reports, 54, 104465. https://doi.org/10.1016/J.JASREP.2024.104465

[22] K. Desjardins, C. Mocuta, A. Dawiec, S. Réguer, P. Joly, J. M. Dubuisson, F. Alves, A. Noureddine, F. Bompard, D. Thiaudière, J. Synchrotron Radiat. 29, 180 (2022) https://doi.org/10.1107/S1600577521012492/GY5028SUP1.AVI

[23] V. Petricek, M. Dusek, L. Palatinus Jana 2006, The Crystallographic Computing System Institute of Physics, Praha, Czech Republic (2006)

[24] G. Murry, Transformations dans les aciers, Techniques de l'ingénieur (1998).

[25] W.D. Callister & D.G. Rethwisch, (2014). Materials Science and Engineering: An Introduction (9th Edition). John Wiley & Sons.

[26] Paul R. Howell, The Pearlite Reaction in Steels Mechanisms and Crystallography: Part I. From H. C. Sorby to R. F. Mehl, Materials Characterization, 40, Issues 4–5, (1998) https://doi.org/10.1016/S1044-5803(98)00024-2

[27] A. Benarosh, Cinétiques de précipitation de carbures dans des alliages bainitiques modèles, Université Paris-Est, 2021.

[28] W. Hao, L. Guoquan, X. Kuangdi, (2022). Pearlite, Structure and Characteristic of. In: Xu, K. (eds) The ECPH Encyclopedia of Mining and Metallurgy. Springer, Singapore. https://doi.org/10.1007/978-981-19-0740-1_191-1

[29] M. Masoumi, D.M.A. Centeno, E.A.A. Echeverri, Arab J Sci Eng (2024). https://doi.org/10.1007/s13369-024-08888-9

[30] G. K. Williamson and W. H. Hall, Acta Mettalurg. 1, 22-23 (1953) https://doi.org/10.1016/0001-6160(53)90006-6

[31] R. Guinebretière, Diffraction des rayons X sur échantillons polycristallins. Instrumentation et étude de la microstructure - 2e édition, Lavoisier.

[32] A. Fedrigo, F. Grazzi, A. R. Williams, T. Panzner, K. Lefmann, P. E. Lindelof, L. Jørgensen, P. Pentz, A. Scherillo, F. Porcher, and M. Strobl, J. Archaeol. Sci. Reports 12, 425 (2017) https://doi.org/10.1016/j.jasrep.2017.02.014

[33] P. Scherrer, Estimation of the Size and Internal Structure of Colloidal Particles by Means of Röntgen. Nachrichten von der Gesellschaft der Wissenschaften zu Göttingen, 2, 96-100, 1918.

[34] A.R. Stokes and A.J.C. Wilson (1944) The Diffraction of X Rays by Distorted Crystal Aggregates-I, Proceedings of the Physical Society, 56, 174. http://dx.doi.org/10.1088/0959-5309/56/3/303

Supplementary Information

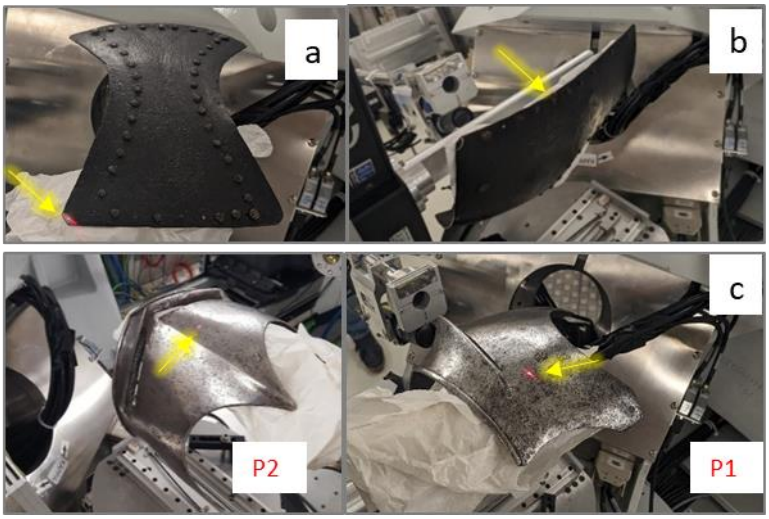

Figure A1. Back plate “PO679.2” (a), left chest plate “PO 679.1” (c) and visor “PO664” (b),the yellow arrow indicates the incident beam impact on the sample.

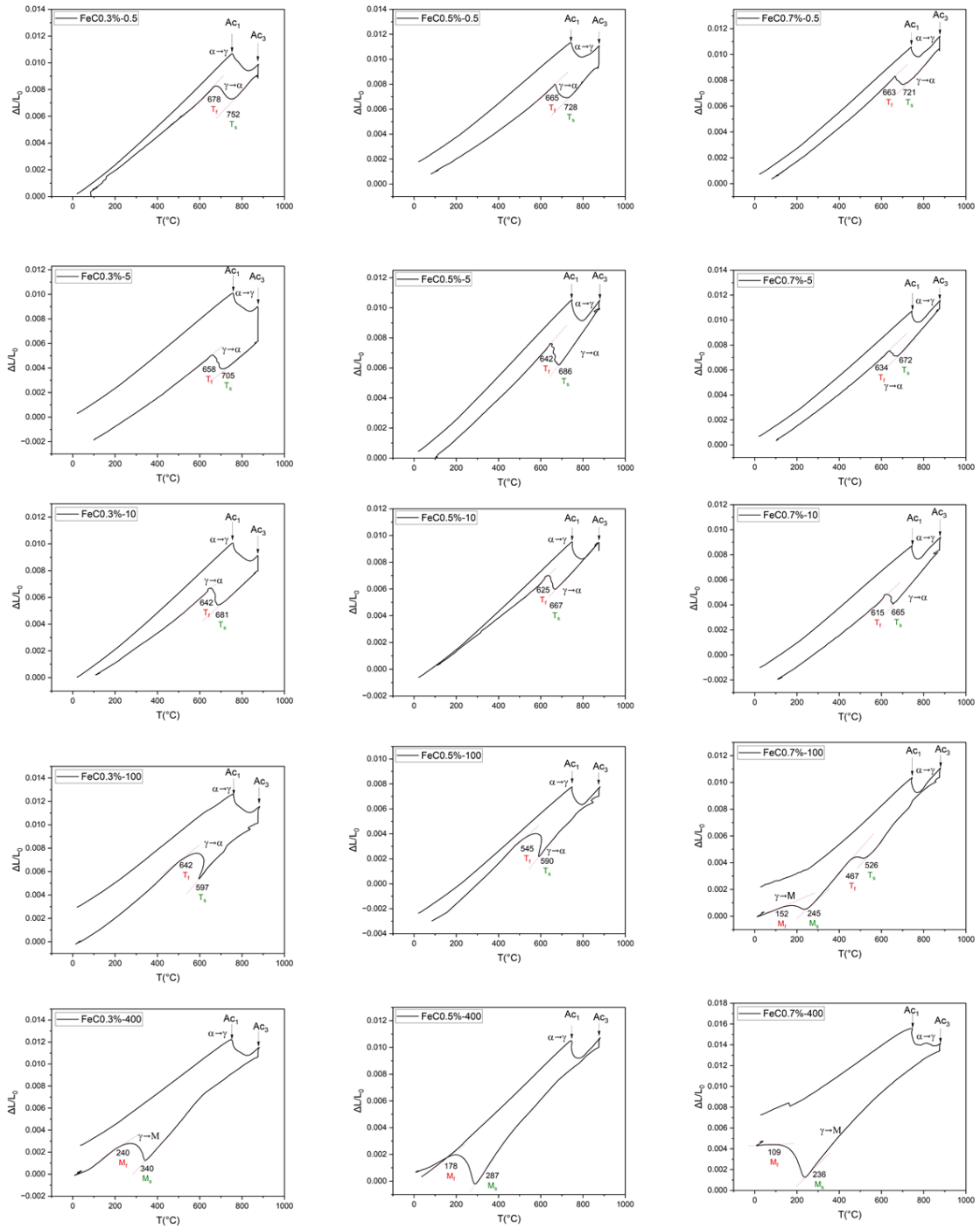

Figure A2: Dilatometric curves of FeC0.3-y, FeC0.5-y and FeC0.7-y model alloys.

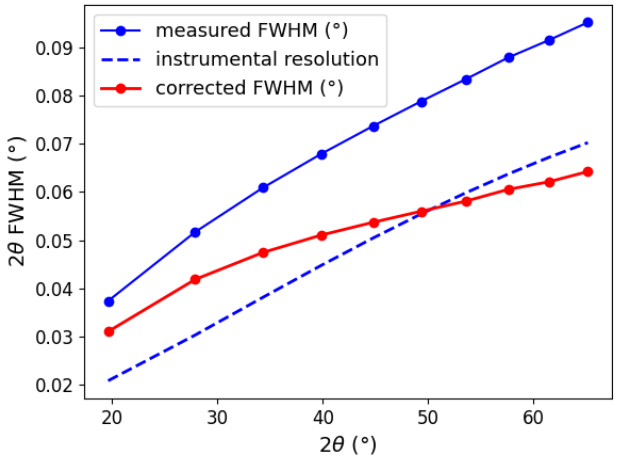

Figure A3: FeC0.3%-0.5 sample: example of the data correction (peak widths deconvolution using the instrumental resolution).

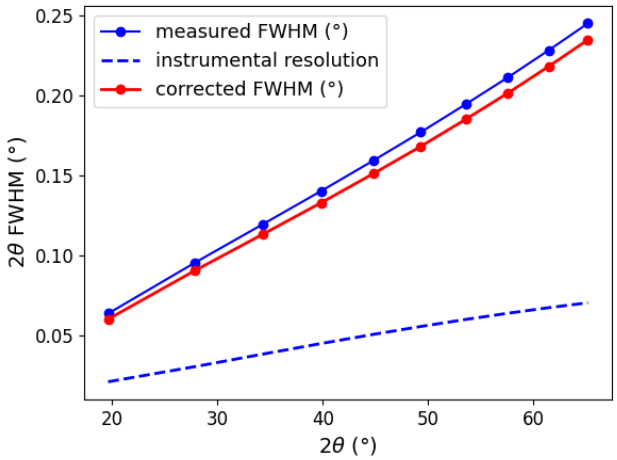

Figure A4: FeC0.5%-100 sample: example of the data correction (peak widths deconvolution using the instrumental resolution).